

BLUEPRINT: Blue-dominant Ly α emission as an evidence of gas inflow in ultra-low-mass galaxies at $z = 3$

Tamal Mukherjee^{1,2}, Zhihui Li³, Tayyaba Zafar^{1,2}, Themiya Nanayakkara⁴, Davide Tornotti⁵, Luca Costantin⁶, and Aalia Imam Uzma^{1,2}

¹ School of Mathematical and Physical Sciences, Macquarie University, NSW 2109, Australia
e-mail: tamal.mukherjee@hdr.mq.edu.au

² Astrophysics and Space Technologies Research Centre, Macquarie University, Sydney, NSW 2109, Australia

³ Center for Astrophysical Sciences, Department of Physics & Astronomy, Johns Hopkins University, Baltimore, MD 21218, USA

⁴ Centre for Astrophysics and Supercomputing, Swinburne University of Technology, P.O. Box 218, Hawthorn, 3122, VIC, Australia

⁵ Dipartimento di Fisica “G. Occhialini”, Università degli Studi di Milano-Bicocca, Piazza della Scienza 3, 20126 Milano, Italy

⁶ Centro de Astrobiología (CAB), CSIC-INTA, Ctra. de Ajalvir km 4, Torrejón de Ardoz 28850, Madrid, Spain

Received XX, XXXX; accepted XX, XXXX

ABSTRACT

We report the detection of a clumpy, blue-dominated Lyman- α ($Ly\alpha$) emission at $z = 3.066$ located in the heart of a cosmic web filament in the MUSE eXtremely Deep Field (MXDF), spatially associated with the formation of two compact star-forming regions revealed by deep JWST/NIRCam imaging. Gas accretion in these regions is indicated by the blue-dominated $Ly\alpha$ profiles, spectral signatures that are rarely observed. Radiative transfer simulation of the $Ly\alpha$ profile using a clumpy multiphase model suggests a radial inflow of gas clumps with a velocity of ~ 100 km/s. Embedded in this $Ly\alpha$ structure, we find that the associated main galaxy dominates the stellar mass budget, while the two compact ultra-low-mass systems ($\log(M_*/M_\odot) = 6.3 - 6.9$) have formed the bulk of their stellar mass in less than 7 Myr. These two components also have high specific star-formation rates, and elevated ionisation parameters, consistent with recent bursty star formation. This system provides direct observational evidence that how gas accretion, most likely from cosmic web, can induce starburst in ultra-low-mass galaxies.

Key words. cosmology: observations–galaxies: evolution–galaxies: high-redshift

1. INTRODUCTION

Galaxies build up their stellar mass over cosmic time by acquiring gas from multiple environmental reservoirs, which include large-scale structures such as the cosmic web (Kereš et al. 2005; Dekel et al. 2009), recycled accretion of gas present in the circumgalactic medium (CGM) (Anglés-Alcázar et al. 2017), as well as accretion from satellite and galaxy mergers (Hafen et al. 2019; Sparre et al. 2022). Despite the theoretical importance of gas accretion in driving galaxy evolution, especially around the peak of cosmic star formation ($z \sim 2-3$), direct observational evidence remains sparse due to challenges such as the low covering fraction and surface brightness of cold, accreting neutral hydrogen (H I) gas filaments.

A powerful observational tracer of gas flows is Ly α $\lambda 1215.67$ Å emission. Due to its resonant nature, the Ly α line is highly sensitive to the kinematics, geometry, and column density of neutral gas, providing key insights into gas exchange between galaxies and their surrounding environments. In most star-forming galaxies, Ly α profiles are asymmetric and redshifted with respect to systemic velocity, a signature commonly interpreted as resonant scattering in outflowing gas. In contrast, infalling or accreting gas can produce blueshifted Ly α peaks, leading to blue-dominated double-peaked Ly α profiles (see Mukherjee et al. 2023; Bolda et al. 2025 and references therein). Such profiles are expected in theoretical models of gas accretion, but are observationally rare. Only a small fraction ($\lesssim 20\%$) of the overall population of double-peaked Ly α emitters (LAEs) are

found to exhibit a dominant blueshifted peak, both observationally (Mukherjee et al. 2026) and in cosmological zoom-in simulation (Blaizot et al. 2023). A recent study of LAEs in the MUSE eXtremely Deep Field (MXDF) though found a notable number of these systems (Vitte et al. 2025), but lack systemic redshift observation to confirm them as inflowing systems. Furthermore, blue-dominated profiles with a main peak followed by a smaller red bump could also arise from backscattering (Mukherjee et al. 2026). Only a handful of blue-dominated LAEs with confirmed systemic redshifts are known to date (Furtak et al. 2022; Marques-Chaves et al. 2022; Mukherjee et al. 2023; Bolda et al. 2025), confirming the presence of accreting gas and highlighting the difficulty of unambiguously identifying inflowing gas in emission.

In this paper, we report the detection of a clumpy blue-dominated Ly α emission at $z = 3.066$ in MXDF, embedded in a cosmic web filament (Bacon et al. 2021) in the Hubble Ultra Deep Field, and spatially associated with two compact star-forming regions. By combining deep MUSE spectroscopy with unprecedented JWST imaging, spectroscopy and spectral energy distribution (SED) modeling, we present rare observational evidence for active gas accretion triggering star formation in ultra-low-mass galaxies. The structure of this paper is as follows. In § 2, we provide details of observations and data. § 3 presents methods carried out to analyse data. In § 4, we present our results, followed by a discussion. Finally, we summarize our results in § 5. Throughout this paper, we assume a standard flat

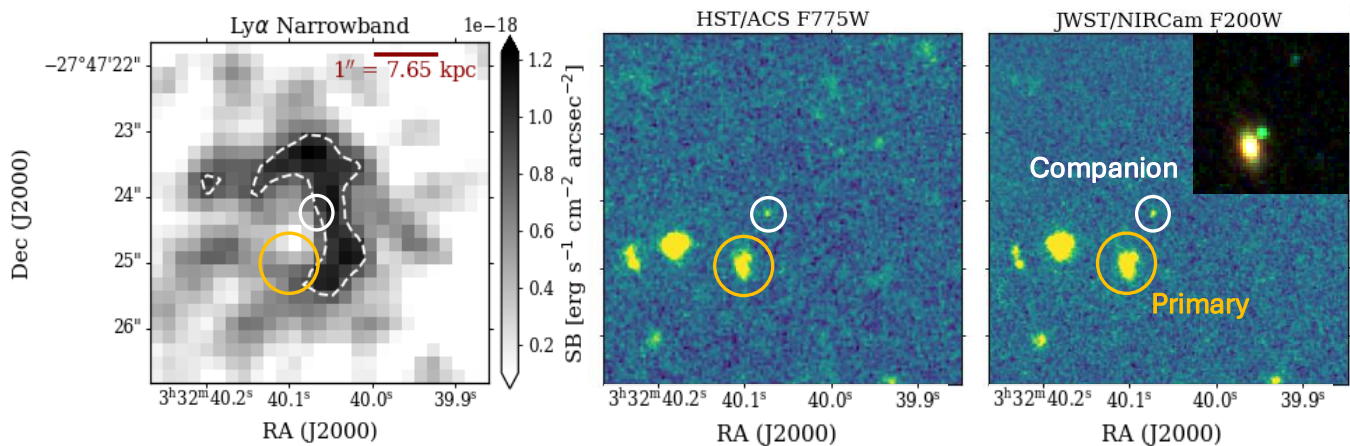


Fig. 1. Continuum-subtracted $\text{Ly}\alpha$ narrow-band image (left) obtained by collapsing the MUSE datacube over 4925–4960 Å, HST/ACS F775W image (middle) and JWST/NIRCam F200W image (right). The white contour in the left panel shows 1.5σ significance level. The yellow circle shows the location of the primary galaxy and white circle represents the same for the companion galaxy. The inset in the top-right corner of the right panel presents a zoomed-in RGB composite of the region containing the three galaxies, constructed using JWST/NIRCam F115W, F200W, and F336W filters.

Λ CDM cosmology with parameters $H_0 = 70 \text{ km s}^{-1} \text{ Mpc}^{-1}$, $\Omega_m = 0.3$ and $\Omega_\Lambda = 0.7$.

2. Data

2.1. MUSE IFU

The primary galaxy and the $\text{Ly}\alpha$ emission are detected in the MUSE data from the MUSE eXtremely Deep Field (MXDF), a 140 h deep MUSE observation located in the Hubble Ultra-Deep Field (Bacon et al. 2021, 2023). The MXDF observations were obtained as part of the MUSE Guaranteed Time Observations (GTO) programme between August 2018 and January 2019, and were carried out using the MUSE ground-layer adaptive optics (GLAO) mode. These are the deepest MUSE data ever obtained, allowing the detection of LAEs down to luminosities of $\sim 10^{40} \text{ erg s}^{-1}$. Details of MXDF data reduction and source catalogue construction are provided in Bacon et al. (2023). In the MXDF, the full width at half maximum (FWHM) of the Moffat point-spread function (Moffat 1969) is approximately $0.6''$ at 4700 Å and $0.4''$ at 9350 Å. The line spread function (LSF) is spatially constant across the field but increases toward the outer regions. The mean MXDF LSF over the full wavelength range is 2.6 Å .

The corresponding blue-dominated double-peaked $\text{Ly}\alpha$ spectrum (MUSE ID: 8360 in the Data Release 2 catalogue, Bacon et al. 2023) is presented in the $\text{Ly}\alpha$ spectral classification study by Vitte et al. (2025). No other emission line is seen in MUSE. The trough between the two $\text{Ly}\alpha$ peaks yields a redshift of $z = 3.066$. The continuum-subtracted $\text{Ly}\alpha$ narrowband image reveals an extended clumpy structure of $\text{Ly}\alpha$ (see the left panel of Fig. 1). Using the publicly available MUSE data products¹, we identify a spatial offset of $0.66''$ between the primary galaxy (MUSE ID: 8497) and the location of maximum $\text{Ly}\alpha$ surface brightness (SB). Furthermore, this $\text{Ly}\alpha$ system is embedded in a cosmic web filament (4 cMpc extended, Bacon et al. 2021).

2.2. HST Imaging

We utilise data from the Hubble Space Telescope (HST) imaging. The data include imaging obtained with the Advanced

Camera for Surveys (ACS) in the four optical filters F435W, F606W, F775W, and F850LP, providing deep rest-frame ultraviolet-to-optical coverage at the redshift of our source. The HST data reveal a faint clump or companion galaxy located at a projected spatial offset of $0.85''$ ($\sim 6.5 \text{ kpc}$ at that redshift) from the primary galaxy (see middle panel of Fig. 1), while the companion itself is offset by $0.2''$ from the $\text{Ly}\alpha$ SB peak. Both the primary galaxy (RAF_ID = 5199) and C (RAF_ID = 5177) are included in the photometric catalogue of Rafelski et al. (2015). The uniform depth and high spatial resolution of the ACS imaging allow robust photometric measurements and morphological characterisation of both components.

2.3. JWST NIRCam and MIRI Imaging

We further combine deep JWST/NIRCam observations of the Great Observatories Origins Deep Survey–South field (GOODS-S) from the JADES (Bunker et al. 2024; Rieke et al. 2023; Eisenstein et al. 2023), and the FRESCO survey (Oesch et al. 2023), providing extensive broad and medium band coverage. Within this region there are imaging data from 14 NIRCam filters: F090W, F115W, F150W, F182M, F200W, F210M, F277W, F335M, F356W, F410M, F430M, F444W, F460M, F480M. Both sources are detected in the NIRCam filters. Further, we identify another resolved component (primary-1 hereafter) associated with the primary galaxy in some of the medium and broad band filters. The RGB composite (see right panel of Fig 1) reveals clear color differences among the three components. The Primary galaxy appears redder, consistent with a relatively older stellar population, whereas primary-1 and the companion appear significantly greener, indicating very young stellar populations. We discuss the resolved photometric extraction for primary-1 in §3.3.

Additionally, we include JWST/MIRI imaging data obtained as part of the MIRI (Rieke et al. 2015; Bouchet et al. 2015; Wright et al. 2023; Dicken et al. 2024) Deep Imaging Survey (MIDIS; PID: 1283) of the Hubble Ultra Deep Field (Östlin et al. 2025). This survey provides some of the deepest mid-infrared observations, enabling sensitive probes of the rest-frame near-infrared emission from distant galaxies (Costantin et al. 2025). The primary galaxy is detected in two MIRI filters (F560W and

¹ <https://amused.univ-lyon1.fr/>

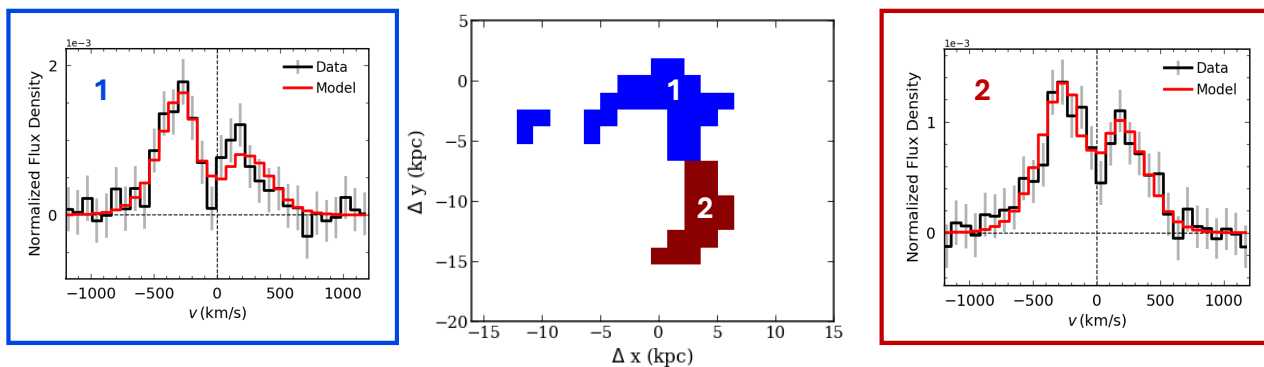


Fig. 2. Radiative transfer modeling of spatially-resolved $\text{Ly}\alpha$ profiles (left and right panel) extracted from Voronoi-binned regions (middle panel), along the direction 1 \rightarrow 2. The observed line profiles are shown in black (with uncertainties shown in gray) and the best-fit models are shown in red. The vertical dashed line represents line centre velocity corresponding to a systemic redshift of $z = 3.066$, obtained from JWST/NIRSpec spectra. Middle panel shows two Voronoi-binned regions displayed on the $\text{Ly}\alpha$ narrowband (NB) image within 1.5σ significance, centred on the pixel with maximum $\text{Ly}\alpha$ surface-brightness.

F770W), while both primary-1 and the companion remain undetected in the MIRI images.

2.4. JWST NIRSpec spectroscopy

The JWST/NIRSpec spectrum of the primary galaxy was obtained as part of the NIRCам–NIRSpec Galaxy Assembly survey of GOODS-S (proposal ID 1286; PI: Luetzgendorf). This programme includes both PRISM spectroscopy and medium- and high-resolution grating/filter combinations, spanning the full wavelength range of $1\text{--}5\ \mu\text{m}$. In this work, we use the spectrum obtained with the medium resolution grating/filter combination, which covers all of the strongest nebular emission lines of interest at medium spectral resolution ($R \sim 1000$), making it well suited for systemic redshift determination. Fitting Gaussian profiles to the $[\text{O III}]$ and $\text{H}\alpha$ emission lines, we measure a systemic redshift of $z_{\text{primary}} = 3.0662$. This redshift is consistent with the spectroscopic redshift reported in the JADES DR4 catalogue (Curtis-Lake et al. 2025; Scholtz et al. 2025) for the primary galaxy (NIRSpec ID: 118073). The slit was positioned such that it covers both the primary galaxy and primary-1. However, we do not detect any additional emission lines associated with primary-1 in either the PRISM or grating spectra. We therefore conclude that primary-1 is at the same redshift as the primary galaxy. The spectrum of the companion was obtained recently as part of the proposal ID 8060 (PI: Egami), with source ID 118266. The corresponding PRISM data were retrieved from the Mikulski Archive for Space Telescopes (MAST) portal². For this source, we estimate a systemic redshift of $z_{\text{companion}} = 3.066$. This confirms that the companion is part of the same system, sharing a consistent redshift with the primary galaxy. The NIRSpec spectra are presented in Fig. A.1 in the Appendix.

3. Methods and analysis

Based on MUSE, HST and JWST observation, this system appears to be a blue-peak dominated $\text{Ly}\alpha$ emission surrounding three galaxies (primary, primary-1 and companion) and indicating gas accretion in multiple spatial locations. In this section, we present methods to study this intriguing system.

² <https://mast.stsci.edu/portal/Mashup/Clients/Mast/Portal.html>

3.1. Spatially-resolved $\text{Ly}\alpha$

We extract a $\text{Ly}\alpha$ spectrum by summing all spaxels with $\text{S/N} > 1.5$ in the MUSE datacube and fit a double-asymmetric Gaussian function similar to Mukherjee et al. (2026). We obtain a total $\text{Ly}\alpha$ flux of $3.97 \times 10^{-18}\ \text{erg cm}^{-2}\ \text{s}^{-1}$. Because of the faintness of the emission, we further implement a Voronoi binning technique to subdivide the halo into regions with reasonable S/N . We perform Voronoi binning on spaxels with $\text{S/N} > 1.5$ in the halo, as shown in the $\text{Ly}\alpha$ NB image. This procedure yields 2 Voronoi-binned regions (Fig. 2) with $\text{Ly}\alpha$ S/N in the range 7.5 - 10. We then extract the $\text{Ly}\alpha$ spectra from each Voronoi-binned region by summing the continuum-subtracted datacube across all spaxels. The spectra from both bins exhibit a blue-dominated double-peaked $\text{Ly}\alpha$ profile, indicating gas inflows. We measure a blue-to-total flux ratio of $\text{B/T} \sim 0.65$ in both bins.

3.2. Radiative transfer modeling using a multiphase clumpy model

We model the spatially resolved $\text{Ly}\alpha$ profiles with a multiphase clumpy radiative transfer model as outlined in Li et al. (2021, 2022); Bolda et al. (2025). In this model, cool ($\sim 10^4\ \text{K}$), spherical H I clumps are assumed to be embedded in and move within a hot ($\sim 10^6\ \text{K}$), ionised inter-clump medium (ICM). The model is characterized by five free parameters: the clump volume filling factor (F_v), which is related to cloud covering factor f_{cl} ; (2) the residual H I number density in ICM ($n_{\text{HI,ICM}}$), which determines the depth of the absorption trough; (3) the velocity dispersion of the clumps (σ_{cl}); (4) a constant radial velocity v_{cl} ; and (5) the H I column density of the clumps. The best-fit model for the spectra from the two Voronoi binned regions are shown in Fig. 2, and the corresponding combined best-fit parameters are listed in Table 1. The best-fit model suggests a clump radial inflow velocity of $v_{cl} \sim 98\ \text{km/s}$.

3.3. Spectral energy distribution modeling using Bagpipes

For companion, we extract photometry by constructing segmentation maps using the JADES NIRCам/F200W image with Photutils (Bradley et al. 2025). The F200W image is adopted as the detection image because it provides the highest signal-to-noise among the available NIRCам observations, enabling ro-

Table 1. Best-fit parameters of Ly α radiative transfer modeling

Parameters	Best-fit value
v_{cl} (km s $^{-1}$)	$-97.82^{+49.40}_{-48.42}$
F_{V}	$0.112^{+0.03}_{-0.04}$
$\log(n_{\text{HI,ICM}}/\text{cm}^{-3})$	$-7.53^{+0.12}_{-0.23}$
$\log(N_{\text{HI,cl}}/\text{cm}^{-2})$	$17.84^{+0.35}_{-0.31}$
σ_{cl} (km s $^{-1}$)	$226.71^{+22.03}_{-39.44}$

bust source segmentation. Local background properties are measured, and the median background is subtracted prior to source detection. We employ the following segmentation parameters for source detection: threshold = 2.5σ per pixel above the background noise, npixels=10. Kron aperture for segment C is set with parameter of 2.0 (KRON). We apply same Kron aperture consistently across all filters, prioritizing the deeper JADES images over the shallower FRESCO images.

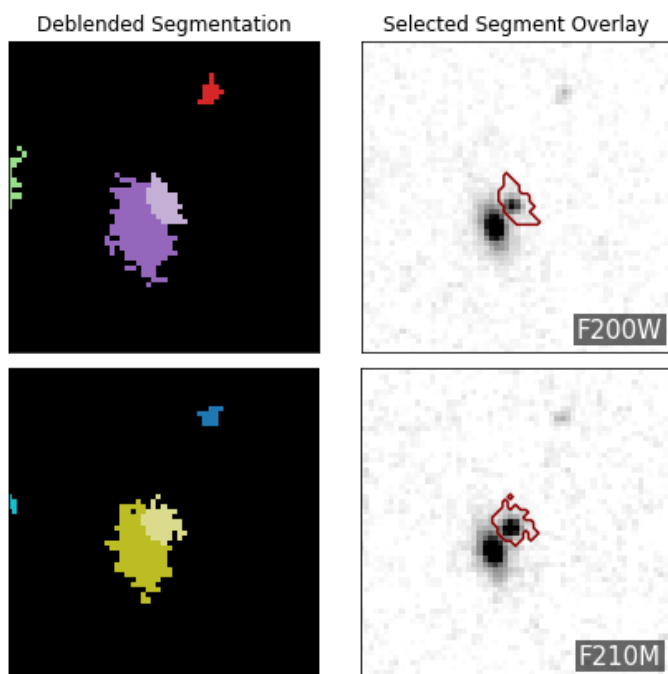


Fig. 3. Deblended segmentation map of the NIRCcam F200W and F210M filter showing segmented region for primary-1 along with the primary galaxy

To extract resolved photometry for clump primary-1, which overlaps with the primary galaxy, we employ a deblended segmentation approach based on a multi-threshold watershed algorithm. The deblending segmentation is performed on the NIRCcam/F200W and F210M filters with the following parameters: npixels = 6, nlevels = 10, and contrast = 0.001. Figure 3 shows the deblended segmentation maps highlighting the identified segment corresponding to primary-1 in two NIRCcam filters. We adopt the deeper F210M image to define the segmentation and obtain resolved photometry by summing the pixel values within the target segment. To ensure consistent photometry across all bands, all other photometric bands are point spread function (PSF)-matched to the F210M PSF and reprojected onto the F210M pixel grid. Fluxes are then measured using identical

segmentation masks across all filters for the primary galaxy and primary-1.

We perform SED fitting on the extracted photometric data using the code Bayesian Analysis of Galaxies for Physical Inference and Parameter ESTimation (or BAGPIPES; Carnall et al. 2018). The model uses a Kroupa (2001) initial mass function and implements the Bruzual & Charlot (2003) stellar population models. A double power-law star formation history is adopted which provides sufficient flexibility to describe both rising and declining star-formation histories (SFH) while avoiding the strong assumptions inherent to simpler parametric forms such as exponentially declining or constant SFHs. The peak time parameter τ is allowed to vary between the Big Bang at 0 Gyr and 15 Gyr later. The total stellar mass formed is sampled over the interval $\log(M/M_{\odot}) \in [1, 15]$, while the stellar metallicity is allowed to vary within 0 to $2.5 Z_{\odot}$. The dust attenuation model of Calzetti et al. (2000) is used, with the visual extinction allowed to vary within the range $0 < A_V < 2$. Nebular emission is included self-consistently, allowing the ionization parameter to vary over $\log U = -4$ to -1 . We additionally allow the escape fraction of ionizing photons, f_{esc} , to vary between 0 and 1. This conservative choice accounts for uncertainties in the coupling between the ionizing stellar population and the surrounding gas, particularly in low-mass systems where ionizing photon leakage may be significant. The physical properties inferred from the SED fitting are presented in Table 2 and the corresponding best-fit SEDs are shown in Fig A.2.

3.4. Emission line diagnostics

For the primary galaxy, strong emission lines such as H β λ 4861, [O III] λ 4959,5007 doublet and H α λ 6563 are robustly detected at S/N > 5 in G235M F170LP filter configuration. In addition, [O II] λ 3728 is detected in G140M F070LP filter. We adopt emission-line flux measurements from the publicly available JADES NIRSpc DR4 emission-line catalogue (Curtis-Lake et al. 2025; Scholtz et al. 2025). Due to the absence of temperature-dependant auroral emission lines such as [O III] λ 4363, we are unable to directly constrain the gas-phase metallicity. We therefore instead employ strong-line metallicity diagnostics. Following Sanders et al. (2024), we use empirical calibrations based on the O3 \equiv [O III] 5007/H β line ratios, in which the gas-phase metallicity is parameterised as a polynomial function of these strong-line ratios. To account for the intrinsic double-valued nature of the O3 diagnostic, we additionally verify the solution using the single-valued O32 calibration. Both diagnostics consistently yield a gas-phase metallicity of $12 + \log(\text{O}/\text{H}) \sim 8.17$.

Additionally, we utilise the prism spectrum of the companion galaxy to obtain line fluxes by fitting Gaussian profiles. The H α based SFR is listed in Table 2. Due to the faintness of the source, only H α and [O III] λ 5007 emission lines are robustly detected, while H β is not directly resolved. We therefore infer the H β flux assuming a standard Case B recombination Balmer decrement ($H\alpha/H\beta = 2.86$). Using the inferred [O III]/H β ratio, we compute the O3 index and apply the same metallicity calibration as adopted for the primary galaxy. The O3 diagnostic yields two degenerate metallicity solutions. Given the ultra-low stellar mass derived from SED fitting, the high-metallicity solution is unlikely in the context of the galaxy mass–metallicity relation. We therefore adopt the low-metallicity branch, corresponding to $12 + \log(\text{O}/\text{H}) \approx 7.16$.

Table 2. Physical properties of galaxies

Galaxy	$\log(M_*/M_\odot)$	$\langle t \rangle_{\text{MW}}$ (Myr)	$\text{SFR}_{\text{SED}} (M_*/\text{yr})$	$\text{SFR}_{\text{H}\alpha} (M_*/\text{yr})$	$12 + \log(\text{O}/\text{H})$	$\log U$
Primary	$8.39^{+0.31}_{-0.12}$	80	$1.78^{+0.34}_{-0.29}$	1.16 ± 0.07	8.17	$-3.059^{+0.178}_{-0.115}$
Primary-1	$6.91^{+0.22}_{-0.21}$	5	$0.086^{+0.007}_{-0.006}$	-	-	$-2.316^{+0.299}_{-0.315}$
Companion	$6.28^{+0.23}_{-0.18}$	7	$0.025^{+0.003}_{-0.003}$	0.27 ± 0.03	7.16	$-1.584^{+0.358}_{-0.340}$

4. Results and discussions

This paper presents the discovery of clumpy blue-dominant Ly α emissions surrounding galaxies at $z = 3.066$.

4.1. Ly α as an evidence of clump radial inflow

Radiative transfer modeling of blue-dominated Ly α profile using the clumpy multiphase model predicts a strong gas inflow with a velocity of ~ 98 km/s. Importantly, this system is located in the heart of a large-scale cosmic web filament, where continuous baryonic inflow from intergalactic filaments is theoretically expected. The derived volume filling factor $F_V = 0.11$ implies a covering factor $f_{cl} \approx 8.4$ for clumps of radius = 100 pc within a simulation sphere of 10 kpc radius. This corresponds to an H I covering fractions effectively close to unity, indicating that nearly all sightlines intersect neutral clumps. This result is consistent with previous observational studies at $z > 3$ suggesting that the H I covering fraction around galaxies with low Ly α SB is close to unity (e.g., Wisotzki et al. 2018). Further, the extremely low residual interclump neutral density, $\log(n_{\text{HI,ICM}}/\text{cm}^{-3}) \approx -7.5$, indicates that most of the neutral opacity resides in discrete clumps rather than in a volume-filling diffuse phase. Therefore these results support a picture in which the neutral CGM is highly fragmented into compact clumps embedded within a mostly ionised medium.

4.2. Stellar populations and star-formation activities

From the SED best-fitting parameters, we find that the primary galaxy dominates the stellar mass budget ($\log M_*/M_\odot = 8.39$), while primary-1 and the companion are $\sim 3.3\%$ and $\sim 0.9\%$ of the stellar mass of the primary galaxy, respectively. The Primary galaxy has $\text{SFR} = 1.78 M_\odot \text{yr}^{-1}$, implying a specific star-formation rate $\text{sSFR} \equiv \text{SFR}/M_* \approx 10^{-8.14} \text{yr}^{-1}$. In contrast, primary-1 and the companion occupy a more extreme regime. Primary-1 has $\log(M_*/M_\odot) = 6.91$, $\text{SFR} = 0.086 M_\odot \text{yr}^{-1}$, and mass-weighted age $\langle t \rangle_{\text{MW}} = 5$ Myr. The Companion is similarly young and bursty, with $\log(M_*/M_\odot) = 6.34$, $\text{SFR} = 0.023 M_\odot \text{yr}^{-1}$, $\langle t \rangle_{\text{MW}} = 7$ Myr. SFRs derived from different diagnostics probe different timescales. While the SED-based SFR traces star formation averaged over longer periods, H α traces much more recent star formation on timescales of ~ 5 – 10 Myr. The higher H α SFR in the companion as compared to SED based SFR therefore suggests a very recent burst of star formation. Both the primary-1 and companion exhibit very high $\text{sSFR} \approx 10^{-7.98} \text{yr}^{-1}$, firmly placing them in the starburst regime (Rinaldi et al. 2025). These sSFRs imply rapid growth (mass-doubling in ~ 0.1 Gyr) and strongly support the interpretation that primary-1 and the companion are experiencing very recent and likely ongoing star-formation episodes.

The inferred ionisation parameters also show a strong progression across the system. The Primary has a relatively modest $\log U = -3.059$, whereas primary-1 has $\log U = -2.316$ and the companion reaches $\log U = -1.584$. Higher U corresponds to a larger ionising photon density relative to the gas density, and is commonly associated with compact star-forming regions hosting very young massive stars. The combination of extremely young ages and high $\log U$ in primary-1 and the companion therefore suggests harder and more intense local ionising radiation fields than in the primary's integrated light. Importantly, these two galaxies are co-spatial with regions that exhibit strong blue-peaked Ly α emission. The coincidence of (i) blue-dominant Ly α profiles and inferred inflow kinematics from modeling, with (ii) very young stellar populations, high sSFR , and elevated ionisation parameters, strongly supports a scenario in which active gas accretion is fueling and triggering the current star-formation episodes in the compact ultra-low-mass substructures. The low gas phase metallicity of the companion further indicates a chemically young and metal-poor interstellar medium consistent with a rapidly assembling low-mass system.

4.3. NFW density profile modeling

To further understand the physical connection between the three galaxies, we examine their dark matter environment using Navarro–Frenk–White (NFW) density profile modeling (Navarro et al. 1997). In this framework, the primary galaxy and the compact primary-1 component are treated as a single dominant system defining the central halo, while the companion is modeled as an independent sub-halo placed at a projected spatial offset of 6.5 kpc. This approach allows us to assess whether the companion is gravitationally embedded within the primary's halo and whether it can remain dynamically distinct.

To construct the NFW profiles, we first estimate the dark matter halo masses associated with the galaxies by converting their stellar masses into halo masses using the stellar-to-halo mass relation of Moster et al. (2013). The halo mass M_{200c} is defined as the mass enclosed within a radius R_{200c} where the mean density is 200 times the critical density of the Universe at the systemic redshift. For each halo, the concentration parameter is computed using the redshift-dependent concentration–mass relation implemented in the CoLossus package (Diemer & Joyce 2019). The corresponding scale radius $r_s = R_{200c}/c_{200c}$ and characteristic density ρ_s were then derived from the standard NFW parametrization. The combined profile is computed by shifting the companion NFW by 6.5 kpc and summing it with the primary NFW at each radius on a common radial grid. The resulting NFW density profiles (Fig. 4) show that the companion is clearly located well inside the virial region of the primary halo. The combined density profile is dominated by the primary at all radii, confirming that the primary galaxy defines the overall gravitational potential of the system. However, the companion's

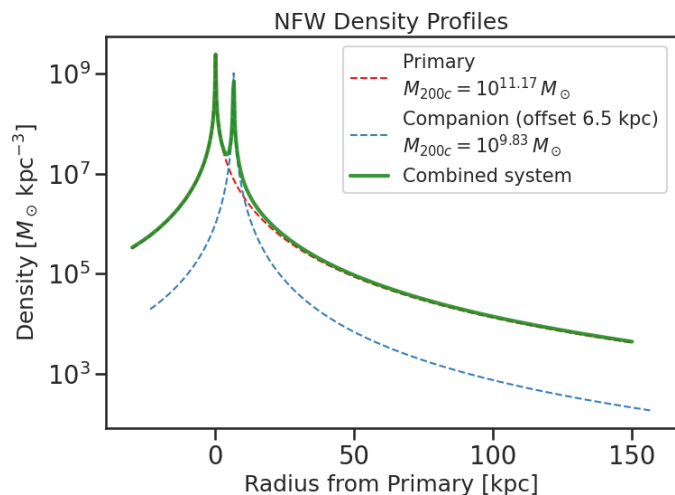


Fig. 4. NFW dark matter density profiles for the system at $z = 3.066$. The red dashed curve shows the NFW profile of the Primary galaxy halo (including the compact Primary–1 component), the blue dashed curve shows the Companion modeled as a sub-halo placed at a projected offset of 6.5 kpc, and the solid green curve shows the combined density profile.

own NFW profile remains well defined and locally distinct, indicating that it survives as a coherent sub-halo rather than being fully disrupted or dissolved into the central halo. This configuration strongly suggests that the system represents an early-stage satellite–host interaction within a common dark matter halo.

4.4. Accretion from cosmic web filament

As mentioned before, the system lies within a large-scale cosmic web filament, where diffuse H I gas is expected to flow along filamentary structures and accrete onto galaxies. The prominent blue peaks in the Ly α profiles and the inflow velocities inferred from modeling are very consistent with this picture. In general, low-metallicity gas from the cosmic web supplies fresh fuel for star formation and galaxy growth at high redshift (Kereš et al. 2005; Dekel et al. 2009). While shock-heated hot-mode accretion of metal-enriched gas may dominate in more massive systems with $\log(M_*) \gtrsim 10.5$ at cosmic noon (Dekel et al. 2009; Bolda et al. 2025), our system hosts low-mass galaxies where relatively cool, metal-poor gas can efficiently accrete along filamentary streams without being shock-heated, providing fresh fuel for star formation. Within this framework, the primary galaxy likely resides near the center of the shared dark matter halo and defines the overall gravitational potential of the system. Its relatively older mass-weighted age, higher metallicity, and lower ionisation parameter suggest a more evolved stage of star formation. In contrast, the compact components primary–1 and the companion may trace localised star-forming regions triggered by cold gas streams feeding the halo. A similar scenario has recently been suggested by Tornotti et al. (2025), who identified LAEs embedded within a cosmic web filament traced by extended Ly α emission in the MUSE Ultra Deep Field (Lusso et al. 2019). Some of their sources exhibit blue-dominated double-peaked Ly α profiles, interpreted as possible signatures of gas accretion from the surrounding intergalactic medium, consistent with the picture suggested for our system.

4.5. Recycled accretion?

An alternative possibility is that some fraction of the accreting gas could be recycled material (Oppenheimer et al. 2010; Anglés-Alcázar et al. 2017). Outflows driven by earlier star formation in the primary galaxy may cool, lose momentum, and subsequently fall back toward the system, where they can fuel new star formation. In this scenario, the recycled gas is expected to preferentially accrete and settle into local gravitational potential minima, such as those associated with compact dark matter sub-halos. This potentially explains their spatial association with the primary galaxy and their elevated star-formation activity. However, with the currently available data we cannot uniquely distinguish between pristine gas accretion from the cosmic web filament and recycled accretion, and both processes may contribute to the gas supply in this system.

5. SUMMARY

Our system provides a unique window into the dynamic processes governing early galaxy formation and evolution. By leveraging the unprecedented capabilities of JWST, we capture a critical phase of galactic assembly, revealing how interactions and gas accretion can trigger star formation in ultra-low-mass galaxies and drive complex gas dynamics. The detection of strong gas inflows within the Ly α filament, together with the emergence of compact star-forming regions, highlights the intricate mechanisms through which galaxies grow at high redshift.

Overall, this system offers a compelling observational example of gas accretion operating across multiple spatial scales within a single dark matter halo, simultaneously sustaining galaxy-wide growth while triggering intense, localised star formation in low-mass components. In this context, this system establishes blue-dominated Ly α emission as a direct probe of cosmic-web-driven baryon inflow and rapid stellar mass growth in faint galaxies.

Future high-resolution studies, particularly those combining multi-wavelength observations with advanced radiative transfer modeling, will be essential for further disentangling the interplay between galaxy interactions, gas accretion, and star formation in the early Universe.

Acknowledgements. TM acknowledges support through the International Macquarie Research Excellence Scholarship Program (iMQRES). TN thanks support through ARC Discovery Project Grant DP230103161. This work is based on observations taken by VLT, which is operated by European Southern Observatory. This work utilizes observational data acquired through the NASA/ESA/CSA James Webb Space Telescope, retrieved from the Mikulski Archive for Space Telescopes (MAST) maintained by the Association of Universities for Research in Astronomy, located at the Space Telescope Science Institute.

Appendix A: Appendix

References

- Anglés-Alcázar, D., Faucher-Giguère, C.-A., Kereš, D., et al. 2017, *MNRAS*, 470, 4698
- Bacon, R., Brinchmann, J., Conseil, S., et al. 2023, *A&A*, 670, A4
- Bacon, R., Mary, D., Garel, T., et al. 2021, *A&A*, 647, A107
- Blaizot, J., Garel, T., Verhamme, A., et al. 2023, *MNRAS*, 523, 3749
- Bolda, C., Li, Z., Erb, D. K., Steidel, C. C., & Chen, Y. 2025, *ApJ*, 982, 54
- Bouchet, P., García-Marín, M., Lagage, P.-O., et al. 2015, *PASP*, 127, 612
- Bradley, L., Sipőcz, B., Robitaille, T., et al. 2025, *astropy/photutils: 2.2.0*
- Bruzual, G. & Charlot, S. 2003, *MNRAS*, 344, 1000
- Bunker, A. J., Cameron, A. J., Curtis-Lake, E., et al. 2024, *A&A*, 690, A288
- Calzetti, D., Armus, L., Bohlin, R. C., et al. 2000, *ApJ*, 533, 682
- Carnall, A. C., McLure, R. J., Dunlop, J. S., & Davé, R. 2018, *MNRAS*, 480, 4379
- Costantin, L., Gillman, S., Boogaard, L. A., et al. 2025, *A&A*, 699, A360
- Curtis-Lake, E., Cameron, A. J., Bunker, A. J., et al. 2025, *arXiv e-prints*, arXiv:2510.01033
- Dekel, A., Birnboim, Y., Engel, G., et al. 2009, *Nature*, 457, 451
- Dicken, D., Marín, M. G., Shivaei, I., et al. 2024, *A&A*, 689, A5
- Diemer, B. & Joyce, M. 2019, *ApJ*, 871, 168
- Eisenstein, D. J., Willott, C., Alberts, S., et al. 2023, *arXiv e-prints*, arXiv:2306.02465
- Furtak, L. J., Plat, A., Zitrin, A., et al. 2022, *MNRAS*, 516, 1373
- Hafen, Z., Faucher-Giguère, C.-A., Anglés-Alcázar, D., et al. 2019, *MNRAS*, 488, 1248
- Kereš, D., Katz, N., Weinberg, D. H., & Davé, R. 2005, *MNRAS*, 363, 2
- Kroupa, P. 2001, *MNRAS*, 322, 231
- Li, Z., Steidel, C. C., Gronke, M., & Chen, Y. 2021, *MNRAS*, 502, 2389
- Li, Z., Steidel, C. C., Gronke, M., Chen, Y., & Matsuda, Y. 2022, *MNRAS*, 513, 3414
- Lusso, E., Fumagalli, M., Fossati, M., et al. 2019, *MNRAS*, 485, L62
- Marques-Chaves, R., Schaerer, D., Álvarez-Márquez, J., et al. 2022, *MNRAS*, 517, 2972
- Moffat, A. F. J. 1969, *A&A*, 3, 455
- Moster, B. P., Naab, T., & White, S. D. M. 2013, *MNRAS*, 428, 3121
- Mukherjee, T., Zafar, T., Nanayakkara, T., et al. 2026, *PASA*, 43, e021
- Mukherjee, T., Zafar, T., Nanayakkara, T., et al. 2023, *A&A*, 680, L5
- Navarro, J. F., Frenk, C. S., & White, S. D. M. 1997, *ApJ*, 490, 493
- Oesch, P. A., Brammer, G., Naidu, R. P., et al. 2023, *MNRAS*, 525, 2864
- Oppenheimer, B. D., Davé, R., Kereš, D., et al. 2010, *MNRAS*, 406, 2325
- Östlin, G., Pérez-González, P. G., Melinder, J., et al. 2025, *A&A*, 696, A57
- Rafelski, M., Teplitz, H. I., Gardner, J. P., et al. 2015, *AJ*, 150, 31
- Rieke, G. H., Wright, G. S., Böker, T., et al. 2015, *PASP*, 127, 584
- Rieke, M. J., Robertson, B., Tacchella, S., et al. 2023, *ApJS*, 269, 16
- Rinaldi, P., Navarro-Carrera, R., Caputi, K. I., et al. 2025, *ApJ*, 981, 161
- Sanders, R. L., Shapley, A. E., Topping, M. W., Reddy, N. A., & Brammer, G. B. 2024, *ApJ*, 962, 24
- Scholtz, J., Carniani, S., Parlanti, E., et al. 2025, *arXiv e-prints*, arXiv:2510.01034
- Sparre, M., Whittingham, J., Damle, M., et al. 2022, *MNRAS*, 509, 2720
- Tornotti, D., Fumagalli, M., Fossati, M., et al. 2025, *ApJ*, 980, L43
- Vitte, E., Verhamme, A., Hibon, P., et al. 2025, *A&A*, 694, A100
- Wisotzki, L., Bacon, R., Brinchmann, J., et al. 2018, *Nature*, 562, 229
- Wright, G. S., Rieke, G. H., Glasse, A., et al. 2023, *PASP*, 135, 048003

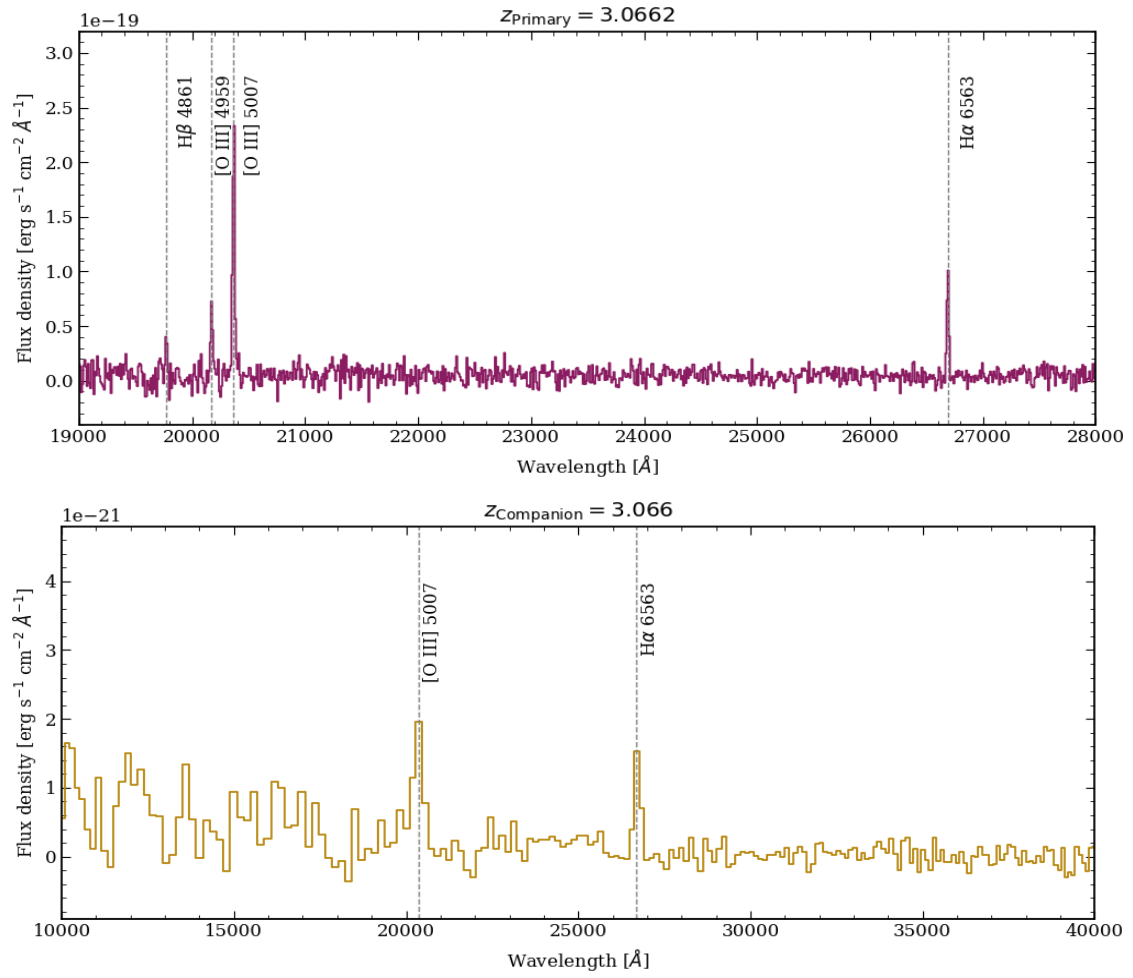


Fig. A.1. Top panel: JWST/NIRSpec medium resolution G235M F170LP spectrum obtained from the location of the primary galaxy (NIRSpec ID = 118073). Bottom Panel: Low resolution PRISM spectrum of companion galaxy.

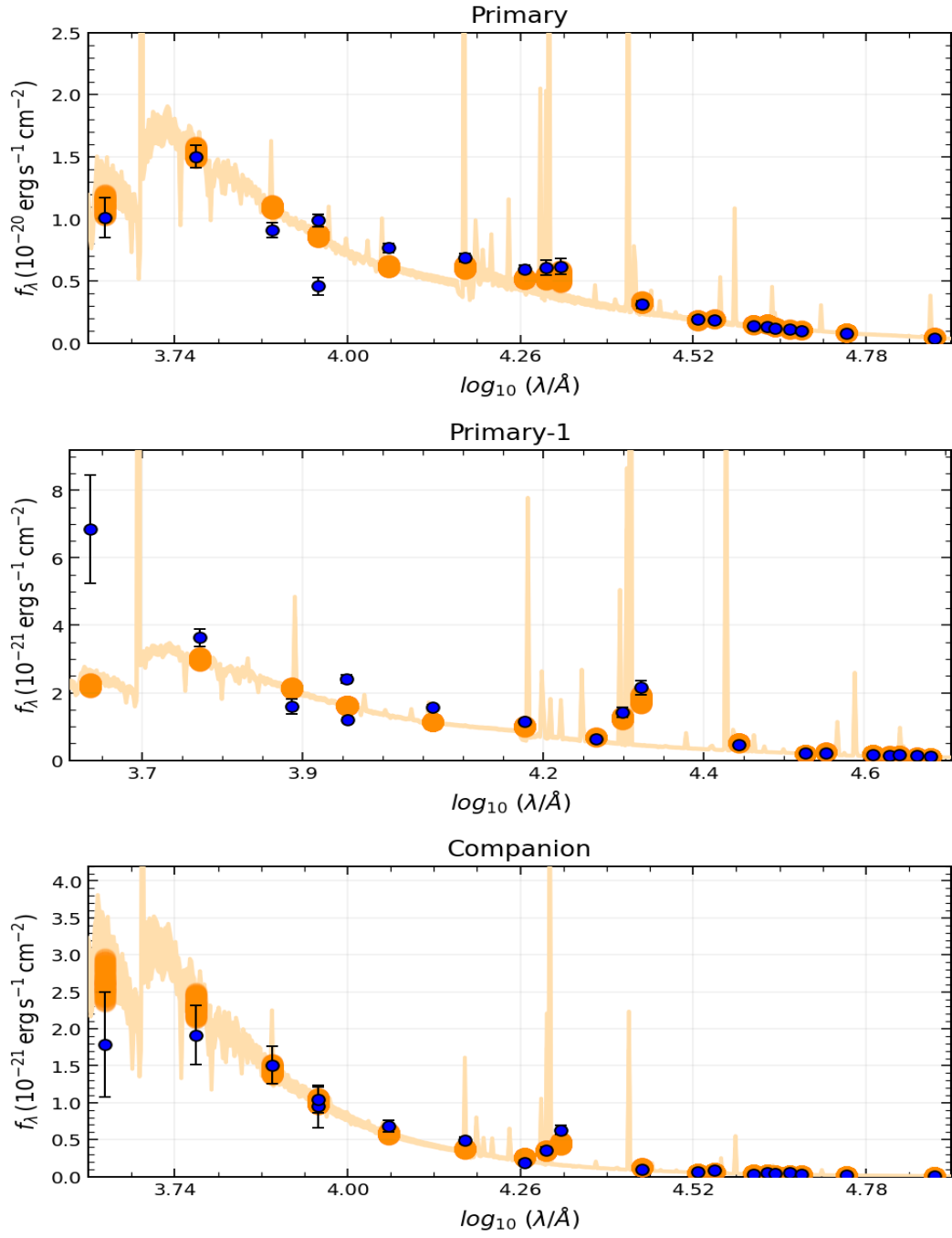


Fig. A.2. Best-fit SED models for the primary, primary-1 and companion galaxy.